# Microstructure of Dry Mortars without Cement: Specific Surface Area, Pore Size and Volume Distribution Analysis

Sahar Seifi, Daniel Levacher, Andry Razakamanantsoa, Nassim Sebaibi

▶ **To cite this version:**

Sahar Seifi, Daniel Levacher, Andry Razakamanantsoa, Nassim Sebaibi. Microstructure of Dry Mortars without Cement: Specific Surface Area, Pore Size and Volume Distribution Analysis. Applied Sciences, 2023, 13 (9), pp.5616. 10.3390/app13095616 . hal-04169274

**HAL Id: hal-04169274**
**https://hal.science/hal-04169274**

Submitted on 18 Dec 2023

**HAL** is a multi-disciplinary open access archive for the deposit and dissemination of scientific research documents, whether they are published or not. The documents may come from teaching and research institutions in France or abroad, or from public or private research centers.

L'archive ouverte pluridisciplinaire **HAL**, est destinée au dépôt et à la diffusion de documents scientifiques de niveau recherche, publiés ou non, émanant des établissements d'enseignement et de recherche français ou étrangers, des laboratoires publics ou privés.

applied sciences

MDPI

*Article*

# Microstructure of Dry Mortars without Cement: Specific Surface Area, Pore Size and Volume Distribution Analysis

**Sahar Seifi [1], Daniel Levacher [1,*], Andry Razakamanantsoa [2] and Nassim Sebaibi [3]**

[1] UMR 6143 CNRS, Unicaen, ComUE Normandie Université, 24 rue des Tilleuls, 14000 Caen, France; sahar.seyfi@gmail.com
[2] Département GERS, Université Gustave Eiffel, CS 4 Route de Bouaye, 44344 Bouguenais, France; andry.razakamanantsoa@univ-eiffel.fr
[3] Builders Lab, Builders École d'Ingénieurs Caen, ComUE Normandie Université, 14160 Epron, France
* Correspondence: daniel.levacher@unicaen.fr

**Abstract:** The evolution of the microstructure of the wastepaper sludge ash-based dry-mortar mixtures is characterized. Mixtures have been prepared with a large volume of wastepaper sludge ash (WSA) and ground granulated blast-furnace slag (GGBS) as a binder matrix mixed with water. Two ratios of water/binder (w/b) = 0.5 and 0.6 were selected. Both of these two industrial by-products are well-known as supplementary cementitious materials in the construction industry and they constitute a convenient replacement for cement. A series of these dry mortars for two ratios w/b were activated by three different chemical activators. They were placed in 4 × 4 × 16 $cm^3$ molds and then compacted at the same compaction energy of 600 kN·m/$m^3$. The influence of water quantity, compaction level and activators on the microstructure of these mortars was investigated by measuring the specific surface area, pore size and volume. Different series of samples have been compared in terms of adsorption/desorption hysteresis and pores network. The influences of water quantity and energy level were first discussed on non-activated dry mortars and this analysis led to the selection of an optimal energy for the comparative study of activated dry mortars. A significant difference in behavior was observed between the studied activators in terms of specific surface area, adsorption property and pore distribution. Then, the microstructure of the three activated dry mortars is observed and analyzed considering the two w/b ratios, the mechanical strength obtained and the type and dosage of activator used. Dry mortars show micropores regardless the quantity of water and the dosage of activator.

**Keywords:** mortar; wastepaper sludge ash; supplementary cementitious material; microstructure; adsorption; specific surface area; pore size distribution

check for updates

**Citation:** Seifi, S.; Levacher, D.; Razakamanantsoa, A.; Sebaibi, N. Microstructure of Dry Mortars without Cement: Specific Surface Area, Pore Size and Volume Distribution Analysis. *Appl. Sci.* **2023**, *13*, 5616. https://doi.org/10.3390/app13095616

Academic Editor: Daniel Dias

Received: 30 March 2023
Revised: 26 April 2023
Accepted: 27 April 2023
Published: 2 May 2023

**Copyright:** © 2023 by the authors. Licensee MDPI, Basel, Switzerland. This article is an open access article distributed under the terms and conditions of the Creative Commons Attribution (CC BY) license (https://creativecommons.org/licenses/by/4.0/).

## 1. Introduction

The recycling of wastepaper sludge ash (WSA) has been the focus of extensive research around the world [1–5]. Numerous reviews on the recycling potential of waste paper sludge ash have shown that the most successful reuses are in the cement industry, construction and road engineering, geotechnical and agriculture applications. In agriculture, wastepaper sludge, whether incinerated or not, can be applied as a soil amendment when it is free of contamination [6]. However, very small volumes of WSA are spread on land. In mortar and concrete production, wastepaper ash replaced a part of cement. In these studies, the amount of WSA was optimized mainly according to the measurements of mechanical strengths. Typically, the WSA amounts range from 5 wt.% to 10.5 wt.% of the cement weight to obtain standard unconfined compressive strength (UCS) values for concrete [7–11]. Beyond that, the UCS resistance decreases but may be suitable for other construction and road materials [12,13] and to increase the volume of recycled WSA. This is also the case for geotechnical applications such as soil stabilization [14], soil erosion protection and backfill materials [15,16] where the required strengths are no longer those

of construction materials. In order to recycle a larger volume of wastepaper sludge ash while maintaining UCS strengths in line with standard concrete and mortar values, recent studies [17–22] have focused on the activation of WSA alone or in combination with other industrial by-products such as granulated ground blast-furnace slag (GGBS). Wastepaper sludge ash and GGBS act as precursors. Different activators are often used separately or in combination for geopolymer concretes, sodium hydroxide and sodium silicate, NaOH and $Na_2SiO_3$, respectively [17–22]. Precursors replace Portland cement, providing green materials. These recent studies mainly concern so-called green concretes, but few consider mortars and even fewer dry mortars. Dry mortars based on activated wastepaper sludge ash have the particularity of avoiding the use of cement, i.e., reducing the carbon footprint, recycling an industrial by-product (WSA) and ensuring water savings.

Therefore, the possibility to use waste paper sludge-ash to be used as raw materials for supplying cementing materials is investigated. The mechanical aspects of waste paper sludge as dry mortar have been studied previously by Seifi et al. [23]. The previous study demonstrates the potential of use of paper fly ash and blast-furnace slag as a substitution for standard cemented material.

The present study will be focused on a deep analysis of the contribution of the waste paper sludge ash and the blast-furnace slag on the microstructure evolution of the dry mortar matrix stabilized with paper fly ash and blast-furnace slag. In fact, the chemical reaction that takes place during the hydration of the binder leads to a greater generation of mesopores, i.e., a structural modification. This structural modification modifies the mechanical properties of the matrix in the short or long term. In order to allow a detailed analysis of the changes that take place, we need a suitable analysis method that allows access to information on the pore structure generated by the hydration of the binders tested. Currently, there is no direct method; therefore, indirect measurement methods are used. The most common method is the fluid or gas injection method: mercury, nitrogen, etc. The mercury intrusion porosimetry (MIP) and the Barrett–Joyner–Halenda (BJH, [24]) pore size and volume analysis are two of the available methods. The MIP method allows for the analysis of pore distribution, especially macropores, and is less accurate in the mesopore area, whereas the BJH method allows a fine analysis of the mesopores. The BJH method has the advantage of providing important information about the adsorption isotherm and the specific surface area of the materials. These different parameters are important and little studied in the literature. BET and BJH methods are successively used to study the microstructure of activated or non-activated dry mortars based on paper fly ash and ground slag [24,25].

The dry mortars produced are dynamically compacted with controlled energy. A first non-activated dry mortar (Mix 1) was subjected to a specific compaction study in order to define an optimal energy level to be used for the activated mortars. Once the optimal energy level was selected, three dry mortars (Mix 2, Mix 3 and Mix 4) were activated for several dosages of activators. These mortars, activated or not, were prepared with two different water contents, namely w/b equal to 0.5 (Mix 1 to Mix 4 mixtures) and 0.6 (Mix 1 to Mix 3 mixtures). The microstructure of all these dry mortars was characterized by means of these two methods of investigation. The results analysis was carried out in order to assess the influence of the compaction energy level on the microstructure (Mix 1 mortars). Then, for the same compaction energy, the role of some parameters is investigated as the water content or the w/b ratio, the influence of the dosage and the nature of the activator on the microstructure of the dry mortar's series (Mix 2 to Mix 4 mixtures) were thoroughly examined and discussed. By relating the specific surface area, pore size and pore distribution, the w/b ratio was optimized, a type of activator was selected and a dosage for dry mortars was recommended. Special attention for activated dry mortars focused on these parameters of the pore state with the mechanical strengths obtained.

The present study aims at identifying the extent to which the processing condition impacts the mechanical performance of the WSA+GGBS mixture. In particular, the compaction energy and the hydric condition of the mix are distinguished. In a second step, the

addition of activating additives in the WSA+GGBS mixture is studied. The evolution of the microstructure parameters generated by the addition of activators and their impacts on the evolution of the mechanical performance of WSA+GGBS are discussed in detail in the present study. Considering the recent study on lime-treated soil [26–29], the effects of the physical–chemical reactions on the mechanical performance of WSA+GGBS are expected to be similar to those of Das et al. [26–29]. The microstructure modification due to the physical–chemical reactions in place is expected to be observed through the evolution of the specific surface of the matrix, the shape of the adsorption isotherms and the evolution of the pore distribution in the compacted matrix. In addition, the study of the microstructure through the coupling of specific surface area measurement, pore size and pore volume distribution is rarely addressed. This is the purpose of this paper.

## 2. Materials and Methods

### *2.1. Raw Materials*

#### 2.1.1. Wastepaper Sludge Ash and Ground Granulated Blast-Furnace Slag

The present study is in the continuity of a previous paper on mechanical performance of dry-mortars made with supplementary cementitious materials [23]. All the raw materials, i.e., supplementary cementitious materials are the same, namely wastepaper sludge ash (WSA) and ground granulated blast-furnace slag (GGBS). The microstructure analysis presented here is based on the mixtures whose mechanical strengths have been reported by Seifi et al. [23].

On one hand, WSA is a residue collected from the paper recycling industry which comes from incineration of two types of raw materials: wastepaper sludge (55%) and, wood and wooden waste (45%). WSA is a grey powder and its median particle size $D_{50}$ = 11.68 µm with binding properties. The oxides composition and some physical parameters of wastepaper sludge ash are presented in Table 1.

**Table 1.** Chemical composition of wastepaper sludge ash and ground granulated blast-furnace slag.

| Oxide (wt.%) | CaO | $SiO_2$ | $Al_2O_3$ | $Fe_2O_3$ | MgO | $K_2O$ | $TiO_2$ | $P_2O_5$ | $Na_2O$ | MnO | $SO_3$ | L.O.I |
|---|---|---|---|---|---|---|---|---|---|---|---|---|
| WSA | 50.70 | 19.90 | 10.40 | 1.17 | 2.49 | 1.01 | 0.60 | - | 0.44 | - | 0.66 | - |
| GGBS | 43.60 | 37.30 | 10.90 | 0.70 | 6.60 | 0.20 | 0.50 | - | 0.30 | - | 0.1 | - |

| Parameters | Particle density ($g/cm^3$) | $D_{50}$ (µm) | pH (-) | SSA-BET ($m^2/g$) | Adsorption cumulative surface area of pores-BJH ($m^2/g$) |
|---|---|---|---|---|---|
| WSA | 2.87 | 11.68 | 11.17 | 2.12 | 1.372 |
| GGBS | 2.94 | 10.49 | 8.93 | 0.70 | 0.370 |

Note: $D_{50}$ median diameter of particle size; SSA specific surface area.

The chemical composition varies and depends on the type of paper and wood combusted during incineration cycle but according to X-ray diffraction results, WSA contains mainly several crystalline phases. Those major crystalline phases are the following: Gehlenite $Ca_2Al_2SiO_7$, Calcite $CaCO_3$, Quartz $SiO_2$, Calcium oxide (lime) CaO and Calcium silicate $Ca_2SiO_4$ [30].

On the other hand, ground granulated blast-furnace slag which is designated as GGBS is a by-product from the blast-furnaces formed during the production of iron. As a matter of fact, granulated slag is attained from molten iron slag by quenching it in high pressure; then, it is further processed into a very fine white powder by drying and grinding, and the final product is called GGBS. Today, ground slag is used as the main constituent of certain types of cement (CEM II, CEM III and CEM V) and as an addition for high-performance longer-lasting concrete. A replacement of 70% is permitted by European standard NF EN 206-1. GGBS as a cement addition has interesting characteristics with a constant composition. The chemical composition and other physical parameters of GGBS are given in Table 1. All the physical properties of WSA and GGBS are reported by Seifi et al. [23].

#### 2.1.2. Sand, Cement and Activators

For a few mortars, i.e., control mortars, one type of cement has been added to the mixtures to investigate its effect on mechanical properties and microstructure. The cement used in present study is CEM I 52.5 N, (EN 197-1). The intended uses for this type of cement relate to the preparation of concrete, mortar, grout and other mixtures destined for the construction and the manufacture of construction products. The chemical composition of this cement is given in Table 2. The main elements are calcium, silicon (54.5% CaO and 19.4% $SiO_2$) as well as aluminum and iron (4.8% $Al_2O_3$ and 3.9% $Fe_2O_3$).

**Table 2.** Chemical composition of cement.

| Oxide (wt.%) | CaO | $SiO_2$ | $Al_2O_3$ | $Fe_2O_3$ | MgO | $K_2O$ | $TiO_2$ | $P_2O_5$ | $Na_2O$ | MnO | $SO_3$ | L.O.I |
|---|---|---|---|---|---|---|---|---|---|---|---|---|
| Cement | 64.50 | 19.40 | 4.80 | 3.90 | 1.20 | 0.81 | 0.30 | 0.30 | 0.11 | 0.00 | 2.60 | 2.20 |

The main phases are alite and belite ($C_3S$ and $C_2S$) which are the major binding phases of Portland cements. Calcium aluminate ($C_3A$) and brownmillerite ($C_4AF$) are also present in the cement. From the point of view of physical properties, the absolute dry density of this type of cement is 3.14 g/cm$^3$ and the Blaine fineness is 4150 cm$^2$/g.

The ISO standard sand (CEN EN 196-1) has been used. Its solid particles density is of 2.65 g/cm$^3$. This sand is a natural siliceous sand, clean and the grains are generally isometric and rounded. Additionally, it ranges between 0.08 and 2.00 mm.

Three different types of activator have been chosen for present study. These activators have proposed by several researchers to investigate the effect of each one of them on the binder matrix (in present study, the binder mixture of WSA and GGBS), on level of hydration and microstructure point of view [31,32]. The chosen activators are $Na_2CO_3$, $Na_2O_3Si$ and $CaCl_2$. They are all in powder form, not harmful to work with, easy to find in the industry market and do not cost too much. All details and information to identify these activators are available in Seifi et al.'s work [23].

### *2.2. Mortar Formulation and Samples Preparation*

The mortar components were mixed according to the EN 196-1 standard for mortars. In the present study, the WSA and GGBS contents are 72 wt.% and 28 wt.%, respectively. Several studies have shown that is the optimum proportion for the mixture which leads to higher compressive resistance, [33]. The mortar mixtures have been made with this binder matrix added with standard sand. These mixtures contain a mass binder of $m_b$ (WSA+GGBS), a mass of sand, $m_s = 3\ m_b$ and a mass of water $m_w$. Ratios of water/binder (w/b) were fixed to 0.5 and 0.6 (Table 3).

Mixtures have been compacted and cast into steel molds (40 × 40 × 40 mm$^3$ prisms). Four different levels of energy per unit of volume of sample have been selected for the reference samples (Mix 1), and the compaction energies are as follows: 400, 600, 800 and 1000 kN·m/m$^3$, see Table 3 and Figure 1. According to the mechanical strength results obtained on reference samples, it has been found that energy E = 600 kN·m/m$^3$ is the optimum level of energy needed, which is also related to normal Proctor energy [34]. All the activated samples (Mix 2, Mix 3 and Mix 4) have been achieved using this level of energy (see Figure 1). In laboratory, different proposed compaction procedures were tamping, dynamic compaction using hammering shocks, instead of hydraulic pressure used in industrial manufacturing, but a compaction process is necessary for manufacturing dry mortars (see Seifi et al. [23]).

**Table 3.** Mortar formulations.

| Components↓ | Mass of Each Components in g | | | | | | | | |
|---|---|---|---|---|---|---|---|---|---|
| | **Mix 1** [(1)] | **Mix 2** | | | **Mix 3** | | | **Mix 4** [(2)] | |
| Sand | 1350 | 1350 | | | 1350 | | | 1350 | |
| WSA | 324 | 324 | | | 324 | | | 324 | |
| GGBS | 126 | 126 | | | 126 | | | 126 | |
| Water w/b =0.5 | 225 | 225 | | | 225 | | | 225 | |
| Water w/b = 0.6 | 270 | 270 | | | 270 | | | - | |
| Activator type → | No | $Na_2CO_3$ | | | $Na_2O_2Si$ | | | $CaCl_2$ | |
| Activator (%) [(3)] | - | 5 | 7.5 | 10 | 2 | 3 | 6 | 2 | 3 |
| Activator mass (g) | - | 6.30 | 9.45 | 12.60 | 2.52 | 3.78 | 7.58 | 2.52 | 3.78 |
| E (kN·m/m$^3$) | 400-600-800-1000 | | 600 | | | 600 | | | 600 |
| $UCS_{28}$ w/b = 0.5 (MPa) [(4)] | 2.4-4.6-5.3-6.2 | 3.6 | 2.9 | 1.3 | 10.3 | 7.7 | 5 | 12.6 | 13.7 |
| $UCS_{28}$ w/b = 0.6 (MPa) [(4)] | 5.9-8.8-9.1-10.4 | 6.1 | 3.7 | 3.3 | 8.8 | 9.0 | 10.5 | - | - |

Note: [(1)] Mix 1 without activator has been compacted for four levels of energy; [(2)] Mix 4 was prepared with only the ratio of 0.5; [(3)] Mass percentage is expressed with GGBS content; [(4)] Averaged value of unconfined compressive strength at 28 days.

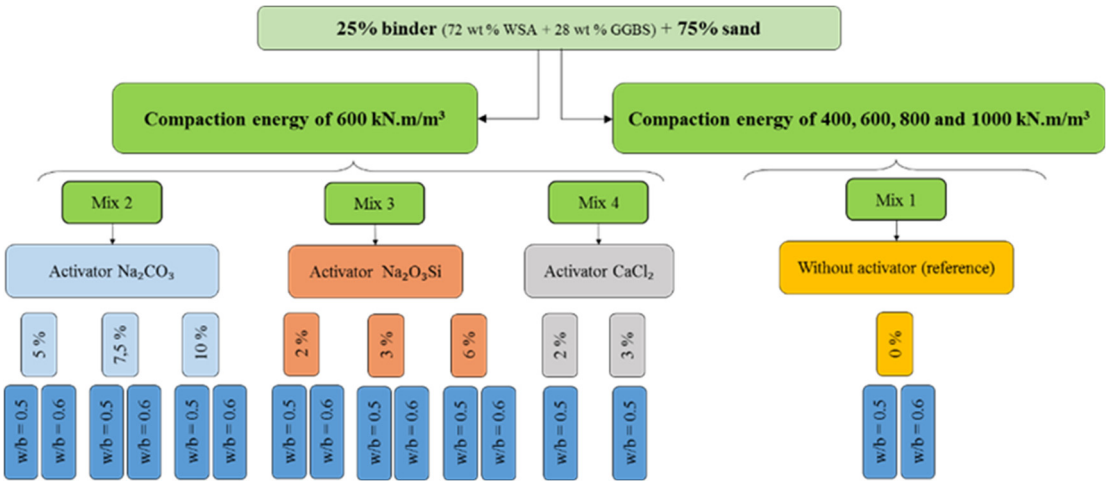


**Figure 1.** Experimental program: composition and preparation of mixtures.

With reference to soil compaction using the normal Proctor test (E = 600 kN·m/m$^3$), which makes it possible to determine the optimum dry density as a function of moisture content, four levels of compaction framing this reference E value were selected. These range from 400 to 1000 kN·m/m$^3$. As mentioned above, the energy corresponding to a better densification, i.e., high strength, of dry mortars is close to the reference E value. This value has therefore been accepted for the different mixes of activated dry mortars. The samples preparation, compaction protocol and the other details on each mixture are reported in Seifi et al.'s work [23].

### *2.3. Methods*

#### 2.3.1. Sample Preparation

A specimen sampled from UCS test was frozen and dried via sublimation. The sample was pre-heated at 50 °C prior the experiment. The relatively low temperature was chosen with the aim of limiting the alteration of the minerals and of the organic matter possibly present in the sample analyzed. Then, the test was carried out at a temperature of 77 K.

2.3.2. Specific Surface Area by BET Method

Brunauer–Emmett–Teller (BET) [25] tests were used for specific surface area (SSA) measurements, isotherm adsorption measurement and pore size distribution characterization. The BET tests were carried out with a Tristar II Plus device. The specific surface area (SSA) designates the relation of the surface of the material to its mass. It is therefore expressed in $m^2/g$ in the international system. It depends mainly on the size of the particles, their shape and their surface condition. A nitrogen ($N_2$) layer is injected into accessible surface inside the compacted specimen. The total of surface covered by the nitrogen molecule corresponds to the specific surface area accessible inside the sample. The measurement and back calculation are carried out 88 times. The SSA results obtained for WSA, GGBS and cement as raw materials are summarized in Table 4.

**Table 4.** Specific surface area of raw materials.

| | WSA | GGBS | Cement |
|---|---|---|---|
| BET ($m^2/g$) | 2.12 | 0.70 | 0.91 |

The BET specific surface area of the cement is 0.91 $m^2/g$ and can be considered a typical value for cements. The specific surface area of GGBS is less than that of the cement. Fly ash (WSA) has a significantly higher surface area than that of cement and GGBS, which should imply a higher water demand than other binders.

2.3.3. Pore Size and Adsorption Isotherm by BJH Method

The pore size distribution and isotherm of adsorption were derived from BET by Barrett, Joyner and Halenda (BJH, [24]) in 1951. Following BET method, nitrogen ($N_2$) layers are injected until full saturation of the soil matrix (adsorption). In addition to the system being fully saturated, the nitrogen injected is pumped by the system until full desaturation (desorption). The characteristic of adsorption/desorption on the accessible pore space connected inside the compacted specimen are determined: isotherm of adsorption, pore size distribution. The BJH method allows one to determine the distribution of the size of the pores in the range of the mesopores and micropores [24,26]. This method is the most applied method for pore-size determination of powder material. The principal assumption of this method is the coexistence of capillary and absorbed gas phases in the cylindrical pores, [35]. The calculation of the pore distribution is based on the step-by-step analysis of the desorption or adsorption branch of the isotherm. The BJH method therefore makes the link between thermodynamic data, the sorption isotherm, and geometric data, intrinsic properties of the solid and the distribution of pore sizes [36].

## 3. Results and Discussion

### *3.1. Isotherm of Adsorption by BJH Method of the Raw Material*

Adsorption/desorption isotherms and the pore size distribution of the raw materials are presented in Figure 2. The curves related to pore distribution have a similar mode, the maximum of all is identic and it is around 0.10 µm. It is also observed that three pore populations exist and the pores of size 0.10 µm dominate the structure. The volume BJH is calculated from the surface of the hysteresis of the nitrogen adsorption/desorption cycle which presents the volume of mesopores and micropores. This volume is relatively high for WSA compared to that of GGBS and cement.

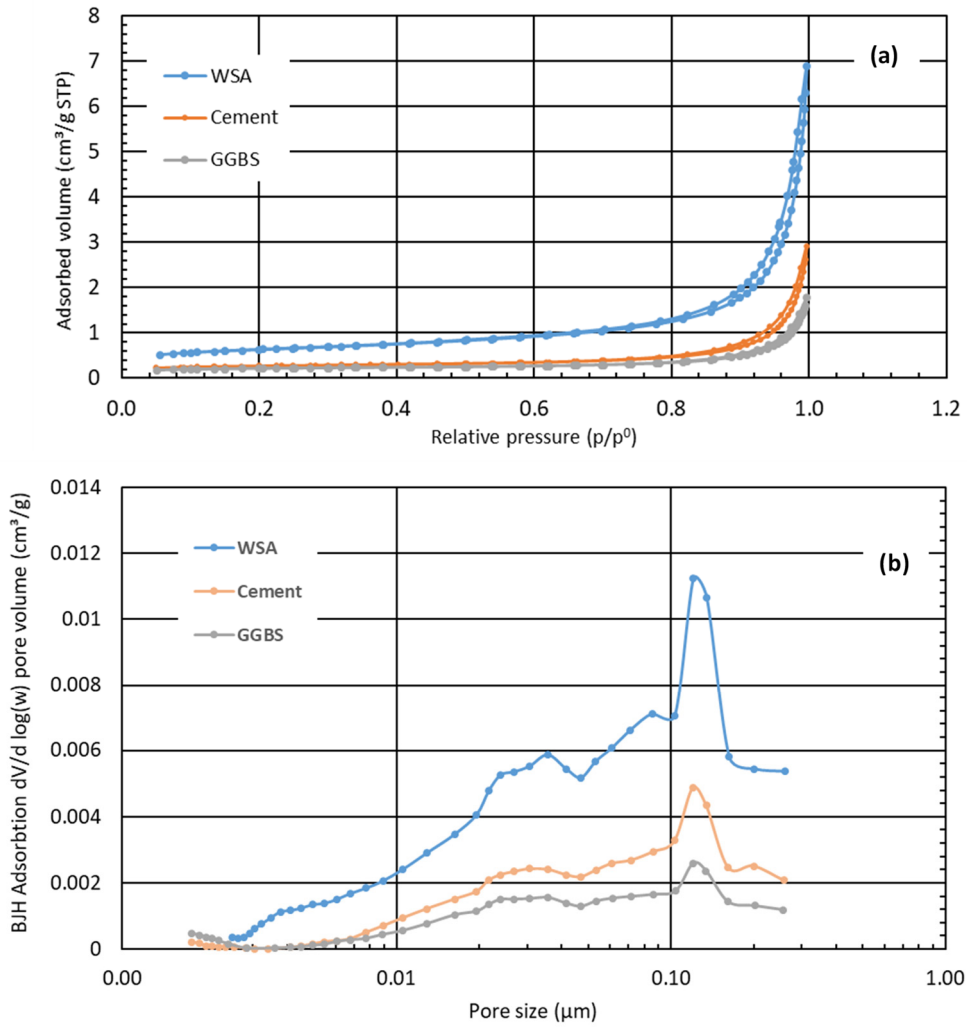


**Figure 2.** (**a**) Adsorption/desorption isotherms and (**b**) pore size distribution of raw materials.

Figure 2a shows the $N_2$ adsorption isotherms of raw materials. The materials are distinguished by their adsorbed volume intensity. The following ranking was observed in increasing order: adsorbed volume of GGBS<Cement<WSA. The adsorption capacity of cement seems to be two times higher than GGBS while that of WSA is eight times higher than GGBS. The hysteresis phenomenon starts to appear from 0.8 P/P°. The difference in adsorption capacity between the different materials demonstrates the hydration affinity. That is, the water attractiveness of the material. In terms of pore distribution, Figure 2b shows a similar trend: the measured pore families are relatively close. The results show that all the tested materials show more pronounced peaks around 0.03 micron, 0.09 micron and 0.12 micron. The difference between the different materials can be observed from the pore intensity. The same rankings as the isotherms are confirmed. The difference in adsorption capacity between the different materials demonstrates the hydration affinity. That is, the water attractiveness of the material.

Table 5 shows the volume of adsorption and desorption of the pores calculated from related isotherms for the three raw materials. The volume adsorbed by the pores of WSA is higher than that of GGBS and cement. This is confirmed by Figure 2, which has a higher area below the curve compared to that of the GGBS and the cement. The hysteresis in Figure 2 shows a very low adsorption/desorption volume; these low values are very close to zero.

**Table 5.** Relationship between pore volume and specific surface area.

| | BJH Adsorption Pore Volume ($cm^3/g$) | BJH Desorption Pore Volume ($cm^3/g$) | Difference ($cm^3/g$) | BET ($m^2/g$) |
|---|---|---|---|---|
| WSA | 0.0089 | 0.0095 | 0.0006 | 2.12 |
| GGBS | 0.0022 | 0.0023 | 0.0001 | 0.70 |
| Cement | 0.0037 | 0.0044 | 0.0007 | 0.91 |

### *3.2. Adsorption/Desorption Isotherms of Dry Mortar References (Mix 1)*

According to the International Union of Pure and Applied Chemistry (IUPAC), a classification system for adsorption isotherms can be categorized into six types based on the isotherm shape [37].

This type of adsorption is a type of physisorption, which is caused by the affinity of the nitrogen gas with the surface of each sample. A material is characterized by its adsorption isotherm curve, that is to say, the quantity of gas adsorbed, as a function of the ratio $P/P_0$, see Figure 3. The quantity of adsorbed gas intruded depends on the ratio $P/P_0$, on the temperature, on the morphology of the solid/gas interface.

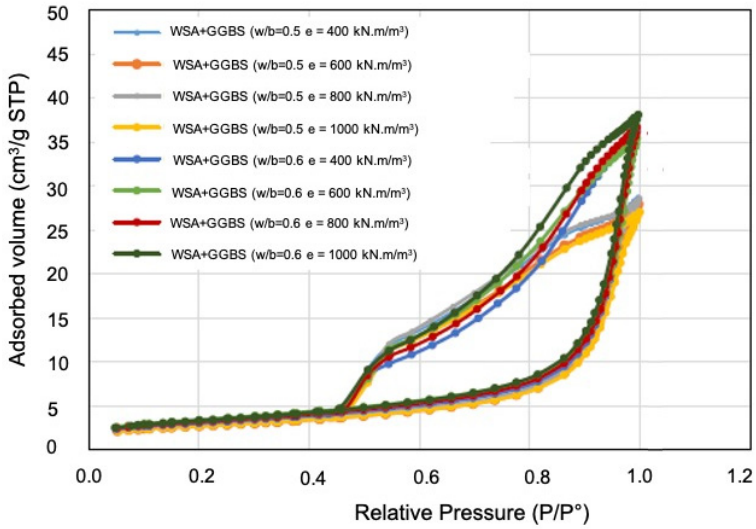


**Figure 3.** Adsorption/desorption isotherms of reference samples Mix 1 with two W/b.

The analysis of the adsorption/desorption isotherms of the reference samples show that their configuration are close to types IV and V (Figure 3). According to the classification of IUPAC, these two types are associated with capillary condensation taking place in mesopores. Considering the classification of the type of hysteresis loop, they are close to types $H_3$ and $H_4$ [38]. The $H_3$ type hysteresis loop can be attributed to capillary condensation taking place in a non-rigid texture but is not characteristic of a specific porosity. This type of loop is, often observed with materials in powder form, or fine aggregates [39]. The $H_4$ hysteresis loop is often observed with materials with micropores in sheets, between which capillary condensation can occur. The isotherm with a hysteretic loop is obtained with mesoporous and/or microporous adsorbents in which capillary condensation occurs. During the desorption if the adsorbed gas condensed by capillarity is trapped, a hysteresis between the sorption and desorption curve is then observed. This effect is observed for all the reference samples.

According to Figure 3, the reference samples prepared with the w/b ratio = 0.5 show completely similar hysteresis for all energy levels and they have the same trends. The isotherm curve of samples in the same series but with the w/b ratio = 0.6, it presents a slightly different hysteresis in terms of height, which shows the volume absorbed.

The specific surface measurements on the reference materials (Table 6) clearly show that the increase in the w/b ratio from 0.5 to 0.6 leads to a clear increase in the specific

surface from 9.63 to 10.59 $m^2/g$ for the lowest compaction energy (400 kN·m/$m^3$) and from 9.35 to 11.53 $m^2/g$ for the highest compaction energy (1000 kN·m/$m^3$). The results show that the effect of compaction on the evolution of the adsorption capacity of the tested mixtures remains visible but negligible compared to the influence of the w/b ratio. The contribution of compaction energy is thus negligible compared to the contribution of hydration.

**Table 6.** Specific surface area BET for Mix 1, (reference samples).

| Mix 1 | Specific Surface Area BET ($m^2/g$) |
|---|---|
| Mix 1 (E * = 400 kN·m/$m^3$), w/b = 0.5 | 9.63 |
| Mix 1 (E = 600 kN·m/$m^3$), w/b = 0.5 | 9.36 |
| Mix 1 (E = 800 kN·m/$m^3$), w/b = 0.5 | 9.68 |
| Mix 1 (E = 1000 kN·m/$m^3$), w/b = 0.5 | 9.35 |
| Mix 1 (E = 400 kN·m/$m^3$), w/b = 0.6 | 10.59 |
| Mix 1 (E = 600 kN·m/$m^3$), w/b = 0.6 | 11.77 |
| Mix 1 (E = 800 kN·m/$m^3$), w/b = 0.6 | 11.09 |
| Mix 1 (E = 1000 kN·m/$m^3$), w/b = 0.6 | 11.53 |

Note: * E = compaction energy applied.

### *3.3. Porosity Distribution of Dry Mortar References (Mix 1)*

The pore size distribution is derived from the BJH model. The most common classification is defined as the measured pore sizes that range from <2 nm to 300 nm, the microporosity refers to pores smaller than 2 nm, the mesoporosity indicates pores from 2 nm to 50 nm, and macroporosity refer to pores with sizes from 50 nm to 300 nm. According to Baroghel-Bouny [40], the dominant pore size in a current cement-based hardened paste is approximately 1.7 nm (micropore), which is associated with the pore size of the C-S-H gel, in fact these pores occur during hydration of gels (C-S-H and CH). On the other hand, it also depends on the W/C ratio (water/cement), the type of cement and the duration of cure. For mortars and concretes which contain aggregates, the pores are larger corresponding to sizes of mesopores and macropores.

Figure 4 shows the influence of the water ratio on the modification of the pore size distribution of the reference sample. In Mix 1 with the ratio w/b = 0.5, they have a monomodal pore size distribution with a peak around 30 nm (0.03 µm) which corresponds to mesopores according to the classification above mentioned. According to Feldman [41], this size has 36% porosity. Feldman has investigated the percentage of porosity of cement-based pastes with different w/b ratio in terms of pore size.

On the other hand, the rise in the w/b ratio = 0.6 generate a multimodal distribution. At least, two populations of pore sizes are present in these samples.

A difference is clearly observed between the 0.5 and 0.6 ratio curves. This difference is illustrated in Figure 4 with arrows. The dominant size remains more or less in the same order of magnitude. For these two formulations with different amounts of water and whatever the level of compaction energy, the pore distribution curves deviate completely, this phenomenon is clearly illustrated in Figure 4.

This phenomenon can be explained by the difference in the specific surface related to these formulations which is presented on Table 6. The formulation prepared with the ratio w/b = 0.6 has a specific surface area greater than that of 0.5. Baroghel-Bouny [40] has shown that when the water/ cement ratio increases in cementitious pastes, the specific surface area also increases. The author observed that there is a linear relationship between the specific surface area and the degree of hydration. Therefore, in our mixes, when the amount of water increases, the hydration reaction is higher and, in fact, the pores appear to be more present in the structure. In Table 7, the average pore size is presented according to the BJH method at the time of nitrogen gas adsorption and desorption. It is shown that the pore size of mixtures with a ratio of 0.6 is slightly larger than that observed with the ratio 0.5. This is in agreement with the curves in Figure 4.

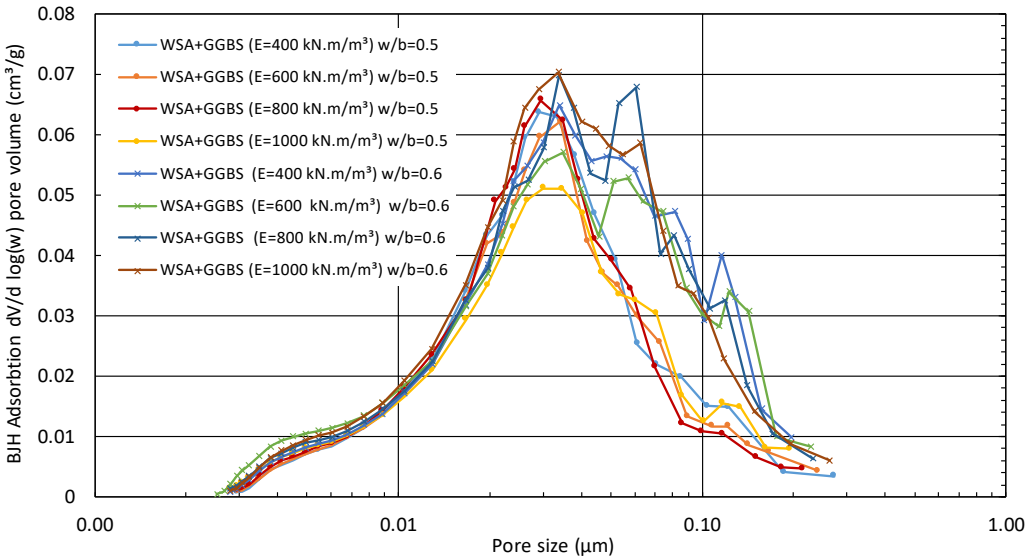


**Figure 4.** Pore size distribution of reference samples (Mix 1).

**Table 7.** Average pore size.

| | BJH Adsorption Pore Size (µm) | BJH Desorption Pore Size (µm) | Difference (µm) |
|---|---|---|---|
| Mix 1 (E * = 400 kN·m/m$^3$), w/b = 0.5 | 0.0198 | 0.0061 | 0.0137 |
| Mix 1 (E = 600 kN·m/m$^3$), w/b = 0.5 | 0.0197 | 0.0062 | 0.0135 |
| Mix 1 (E = 800 kN·m/m$^3$), w/b = 0.5 | 0.0191 | 0.0060 | 0.0131 |
| Mix 1 (E = 1000 kN·m/m$^3$), w/b = 0.5 | 0.0191 | 0.0061 | 0.0130 |
| Mix 1 (E = 400 kN·m/m$^3$), w/b = 0.6 | 0.0228 | 0.0079 | 0.0150 |
| Mix 1 (E = 600 kN·m/m$^3$), w/b = 0.6 | 0.0206 | 0.0072 | 0.0134 |
| Mix 1 (E = 800 kN·m/m$^3$), w/b = 0.6 | 0.0222 | 0.0067 | 0.0146 |
| Mix 1 (E = 1000 kN·m/m$^3$), w/b = 0.6 | 0.0218 | 0.0073 | 0.0145 |

Note: * E = compaction energy applied.

### *3.4. Adsorption/Desorption Isotherms of Activated Dry Mortars (Mix 2, Mix 3 et Mix 4)*

This section present the test results of the samples activated by different activators. These samples are mortars prepared with three types of activators: $Na_2CO_3$, $Na_2O_3Si$ and $CaCl_2$. The isothermal curves thus obtained are presented in Figures 5–7. The isotherms relating to the samples with the addition of sodium carbonate activator show a clear difference in the volume adsorbed.

As presented in Figure 5, when 5% to 10% $Na_2CO_3$ is added, there is a decrease in the volume of $N_2$ adsorbed from 28 cm$^3$/g (Figure 3) to 20 to 23 cm$^3$/g, respectively. The increase of 5% of $Na_2CO_3$ leads to a slight increase in the adsorbed volume. For the same formulation and implementation, the increase in the w/b ratio from 0.5 to 0.6 leads to a significant increase in the adsorbed $N_2$ volume. The increase is 12 cm$^3$/g for 5% and 10 cm$^3$/g for 10% $Na_2CO_3$. However, the hysteresis volume seems to be little impacted by the addition.

This phenomenon is well-explained in the above Figure 3 for references samples. The "ink bottle" effect is more present for samples prepared with a higher amount of water, see Figure 5.

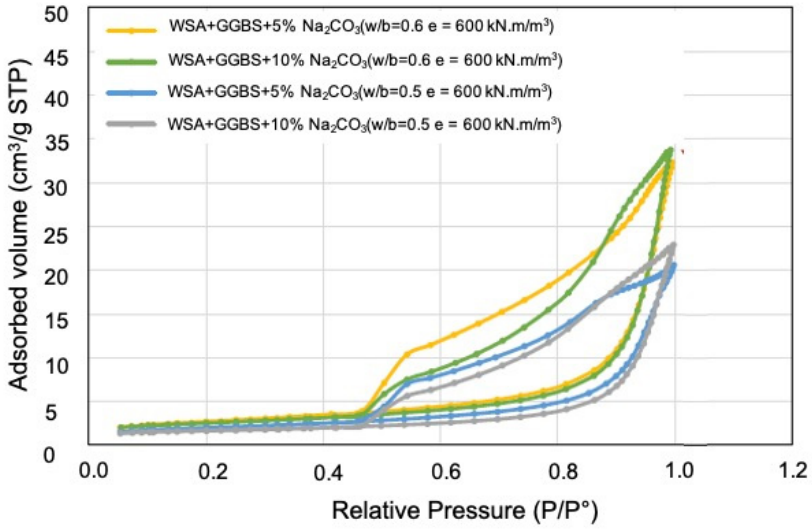


**Figure 5.** Adsorption/desorption isotherms of activated samples Mix 2 with two W/B ratios.

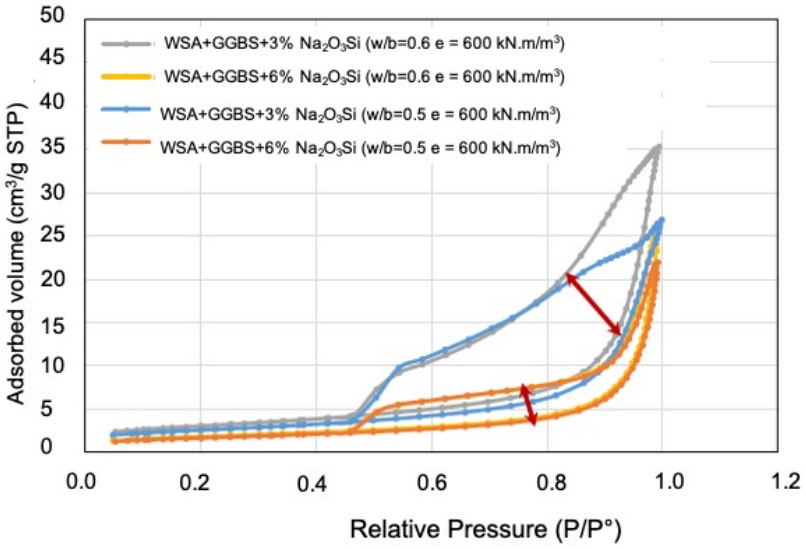


**Figure 6.** Adsorption/desorption isotherms of activated samples Mix 3 with two W/B ratios.

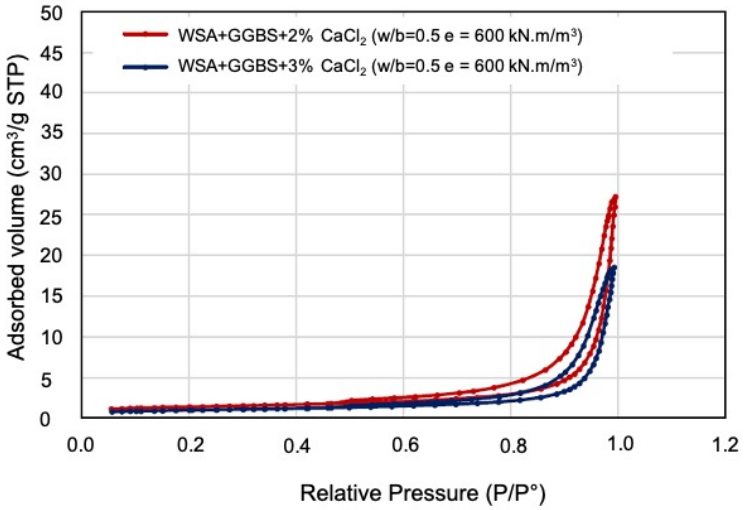


**Figure 7.** Adsorption/desorption isotherms of activated samples Mix 4.

This mechanism of interaction is a little different for samples activated by sodium metasilicate. When 6% $Na_20_3Si$ is added for the WSA+GGBBS mixture and a w/b = 0.5 to 0.6, then, an increase in $N_2$ adsorbed volume is observed with very little impact on the hysteresis evolution. This indicates that the kinetics of $N_2$ restitution is very close.

If we compare the mixtures containing WSA+GGBS with 3% and 6% $Na_2O_3Si$, for the same w/b:0.5 or 0.6 ratio, increasing the concentration of $Na_2O_3Si$ leads to a significant decrease in the volume of hysteresis and the volume of adsorbed $N_2$.

A 3% addition of $Na_2O_3Si$ results in an increase in the volume of the hysteresis compared to the reference mixture Mix 1. Increasing the concentration to 6% leads to a significant decrease in the volume of the hysteresis and the volume of adsorbed $N_2$. This decrease indicates a certain ease of $N_2$ to leave the porous matrix. The amount of adsorbed $N_2$ also decreased drastically. This decrease indicates a decrease in the accessible network volume in the porous matrix.

This information is also coherent with the specific surface area values presented in (see Table 8). The specific surface area values decrease with the raise of $Na_2O_3Si$ concentration whatever the ratio w/b selected.

**Table 8.** Specific surface area BET for Mix 2, Mix 3 and Mix 4 (activated samples).

| Mix 1 | Specific Surface Area BET ($m^2/g$) |
|---|---|
| Mix 2 (5% $Na_2CO_3$), w/b = 0.5 | 6.91 |
| Mix 2 (10% $Na_2CO_3$), w/b = 0.5 | 5.63 |
| Mix 2 (5% $Na_2CO_3$), w/b = 0.6 | 9.41 |
| Mix 2 (10% $Na_2CO_3$), w/b = 0.6 | 8.75 |
| Mix 3 (3% $Na_2O_3Si$), w/b = 0.5 | 9.01 |
| Mix 3 (6% $Na_2O_3Si$), w/b = 0.5 | 5.88 |
| Mix 3 (3% $Na_2O_3Si$), w/b = 0.6 | 10.64 |
| Mix 3 (6% $Na_2O_3Si$), w/b = 0.6 | 6.43 |
| Mix 4 (2% $CaCl_2$), w/b = 0.5 | 4.73 |
| Mix 4 (3% $CaCl_2$), w/b = 0.5 | 3.33 |

Figure 7 shows the curves with very little hysteresis obtained for the samples with the addition of calcium chloride as activator for a ratio w/b = 0.5 (Mix 4).

The increase of 1% $CaCl_2$ leads to a decrease in the volume of adsorbed $N_2$ from 28 to 17 $cm^3/g$. The volume of hysteresis seems to be little impacted. On the other hand, the intensity of the adsorbed $N_2$ volume is six times higher than the volumes measured on the raw materials.

These two curves have a very low adsorption/desorption hysteresis loop compared to the samples activated by the two previous activators. Their specific surface areas are also low according to the data in Table 8.

All isotherms of Mix 2, Mix 3 and Mix 4 exhibit hysteresis loops at $P/P_0 > 0.5$; this is related to the capillary condensation in the interparticle voids. The linear section corresponding to $P/P_0$ = 0.05–0.2 is due to the sorption of nitrogen on the surface of the mesopores and the external surface of particles, mesopores will be filled at around $P/P_0$ = 0.3–0.4. Then, the second linear section at $P/P_0$ = 0.4–0.05 is due to the sorption of nitrogen on the external surface of particles.

In summary, when 5% to 10% $Na_2CO_3$ is added, a decrease in the volume of adsorbed $N_2$ is observed. For the similar formulation and implementation, the increase in the w/b ratio from 0.5 to 0.6 leads to a significant increase in the volume of $N_2$ adsorbed. The increase is 12 $cm^3/g$ for 5% and 10 $cm^3/g$ for 10% $Na_2CO_3$. The volume of hysteresis seems to be little impacted by the addition.

When 6% $Na_20_3Si$ is added, for the mixture of WSA+GGBBS and a w/b ratio = 0.5 to 0.6, then, an increase in adsorbed volume is observed with very little impact on the evolution of hysteresis. For the same ratio w/b:0.5 or 0.6, increasing the concentration of $Na_2O_3Si$ leads to a significant decrease in the volume of hysteresis and the volume of $N_2$

adsorbed. Increasing 1% $CaCl_2$ results in a decrease in the volume of adsorbed $N_2$ from 28 to 17 $cm^3/g$. Hysteresis seems to be little impacted.

### *3.5. Porosity Distribution of Activated Dry Mortars (Mix 2, Mix 3 and Mix4)*

Figure 8 shows the curves for samples activated with three types of activators and the two w/b ratios. All the curves show a size distribution of the multimodal pores. In Figure 8a, we observe four pore families for the w/b = 0.6 ratio regardless of the $Na_2CO_3$ dosage and three pore populations for the w/b = 0.5 ratio. However, for all cases, the dominant pore size is between 0.03 and 0.04 µm; these are mesopores.

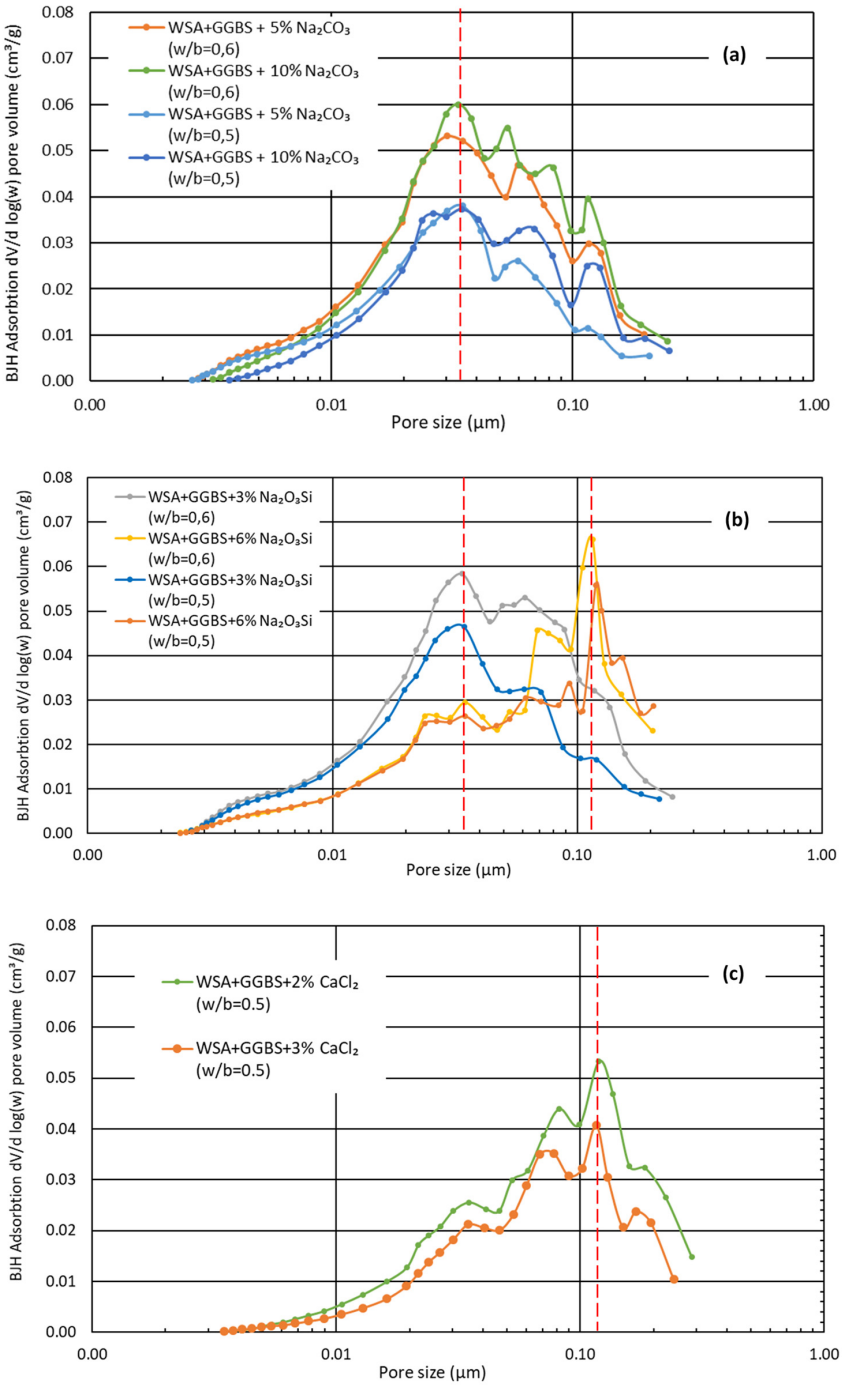


**Figure 8.** Pore size distribution of activated samples: (**a**) Mix 2 with $Na_2CO_3$; (**b**) Mix 3 with $Na_2O_3Si$; (**c**) Mix 4 with $CaCl_2$.

According to the total volumes of $N_2$ adsorbed by the pores (see Table 9), the sample containing 5% $Na_2CO_3$ with the ratio of w/b = 0.5 has a low value of adsorption (0.0304 $cm^3/g$) compared to the other samples in this series with addition of $Na_2CO_3$. This is in good agreement with the related curve of this sample where the area under the curve is less compared to the others (see Figure 8a, curve in blue). The area of the curve is representative of the volume of voids in the structure.

**Table 9.** Specific surface area BJH for Mix 2, Mix 3 and Mix 4 (activated samples).

| Mix 1 | BJH Adsorption Pore Volume ($cm^3/g$) | BJH Desorption Pore Volume ($cm^3/g$) | Difference ($cm^3/g$) | Rc (MPa) | Specific Surface Area BET ($m^2/g$) |
|---|---|---|---|---|---|
| Mix 2 (5% $Na_2CO_3$), w/b = 0.5 | 0.0304 | 0.0436 | 0.0132 | 3.57 | 6.91 |
| Mix 2 (10% $Na_2CO_3$), w/b = 0.5 | 0.0343 | 0.0477 | 0.0134 | 1.35 | 5.63 |
| Mix 2 (5% $Na_2CO_3$), w/b = 0.6 | 0.0488 | 0.0689 | 0.0201 | 6.10 | 9.41 |
| Mix 2 (10% $Na_2CO_3$), w/b = 0.6 | 0.0527 | 0.0677 | 0.0150 | 3.32 | 8.75 |
| Mix 3 (3% $Na_2O_3Si$), w/b = 0.5 | 0.0397 | 0.0581 | 0.0184 | 7.71 | 9.01 |
| Mix 3 (6% $Na_2O_3Si$), w/b = 0.5 | 0.0342 | 0.0412 | 0.0070 | 5.02 | 5.88 |
| Mix 3 (3% $Na_2O_3Si$), w/b = 0.6 | 0.0550 | 0.0708 | 0.0158 | 9.02 | 10.64 |
| Mix 3 (6% $Na_2O_3Si$), w/b = 0.6 | 0.0405 | 0.0471 | 0.0066 | 10.55 | 6.43 |
| Mix 4 (2% $CaCl_2$), w/b = 0.5 | 0.0402 | 0.0446 | 0.0044 | 12.57 | 4.73 |
| Mix 4 (3% $CaCl_2$), w/b = 0.5 | 0.0288 | 0.0304 | 0.0016 | 13.65 | 3.33 |

According to Figure 8a, addition of 5% $Na_2CO_3$ results in a reduction in pore volume $0.20 > p > 0.035$ micron. Increasing the w/b ratio by 0.1 results in an increase in pore volumes in the same range of 0.02 $cm^3/g$. The behavior of samples treated with $Na_2O_3Si$ is particularly remarkable (Figure 8b). The addition of the $Na_2O_3Si$ allows for a shift in the peaks of the distribution curve (0.034 micron) towards larger-pore families (0.15 micron). At last, the addition of 1% more of $CaCl_2$, allows one to lower the pore volume by 0.01 $cm^3/g$.

To establish a link between the mechanical strength and the adsorption capacity of each sample, it is necessary to relate the values of the BET specific surface area and the values of the difference in volume of adsorption/desorption of the pores. In this series of samples, the one with 5% $Na_2CO_3$ and ratio of w/b = 0.6, shows a large difference between the adsorption volume and the pore desorption volume of 0.0201 $cm^3/g$. Moreover, this sample has a high specific surface area. This suggests a very small pore size and the possibility of gas/liquid retention in the pores, and consequently a high mechanical resistance. This has been demonstrated by measuring the highest compressive strength of this series, where a value of 6.10 MPa was obtained.

In Figure 8b, the pore distribution graphs for the samples activated by $Na_2O_3Si$ are plotted. The dominant pore size for the dosage of 6% is larger than that with 3%; this size corresponds to 0.1 and 0.03 µm, respectively. The sample activated by 3% $Na_2O_3Si$ has a higher adsorption volume than the others (0.0550 $cm^3/g$) which corresponds to the volume of voids of material at the time of adsorption. This sample has a fairly high specific surface area, and, this results in a high resistance (compressive strength of 9.02 MPa has been measured). One can conclude that there exist several small pores.

On Figure 8c, a distribution in size of the multimodal pores is also observed, for which at least three populations of size of the pores are present. The sample activated by 3% $CaCl_2$ shows a very low adsorption volume which is related to the volume of voids in the material. From the small specific surface area of this sample and the small difference in adsorption/desorption volume, it can be concluded that there are pores that are not necessarily small, but they are in small quantities. In addition, this sample has the highest mechanical strength in this sample series.

The impact of microstructure evolution on UCS evolution is different depending on the nature of each additive.

The addition of $Na_2CO_3$ increases the pore volume. The increase in pore volume is accompanied by a drop in the compressive strength UCS. The UCS value is relatively higher (6.10 MPa) with a w/b of 0.6 compared to 0.5 but an average drop of 3 MPa is recorded on the tested formulations.

The addition of $Na_2O_3Si$ decreases the pore size. For an w/b ratio of 0.5, a decrease in UCS of 2 MPa is observed. An inverse mechanism occurs with a w/b of 0.6. The gain in UCS is 1.5 MPa.

For $CaCl_2$, the highest compressive strength is recorded among the different activators used. The addition of $CaCl_2$ seems to close the pores and act positively on the UCS value. A gain of 1 MPa is recorded.

Several factors can contribute to the modification of hysteresis. The presence of trapped gas and its ability to exit are the most important; however, the contact angle and geometry of the pores also play a non-negligible role. The hysteresis phenomenon is due to the irregular distribution of the size of the pores, which are generally voids of variable shape interconnected by smaller passages and also the "ink bottle" effect retains an amount of fluid/gas not negligible in the pores during desorption. This effect is all the more important as the variation in section in the pore is large. This is the reason why adsorption/desorption isotherms in the form of hysteresis are observed, especially for cementitious materials [42]. The gas retention capacity of the reference samples with the ratio w/b = 0.6 occurs to be higher than those of the ratio 0.5; the loop is larger than those observed with the ratio 0.5.

This observation is also confirmed by the specific surface area values determined for each sample (see Table 6). The larger the specific surface area, the more the demand for the quantity of water increases per sample. The values observed are around 11 $m^2/g$. Then, the more the number of fluid molecules increases, the more the risk of being trapped in the pores increases; thus, the isothermal effect with hysteresis is more present.

The main contribution of the present research work deals with the microstructure modification as the first product of hydration of the binder. The contrasting contribution of microstructure development on the mechanical strength of the material is observed. The different microstructure pattern generated by each mixture and its correlation with the specimen UCS value are intimately linked to the nature of additives and to the hydration mechanism. The mechanical strength of each hydration product depends also to the mechanical properties of the pores structure generated. Then, it could be an interesting issue to provide further information on the elastic properties of the pore matrix generated by each additive: binder and activators.

## 4. Conclusions

Recycling of wastepaper sludge ash WSA in large volumes in dry mortars can be carried out up to 72%. This constitutes another beneficial use of WSA apart from agronomic spraying or road sublayers.

Replacing cement with two industrial by-products, i.e., wastepaper sludge ash and ground granulated blast-furnace slag GGBS, in mortars is possible by using activators in low dosages. The strengths obtained depend on the water/binder matrix ratio (w/b and b = WSA+GGBS), compaction energy applied for dry mortars, type and dosage of activators. Analyzing the microstructure allows one to optimize these last parameters.

Among the different level of energy of compaction, the optimal energy for a dry mortar consisting of 72% WSA and 28% GGBS is around 600 $kN \cdot m/m^3$ 600. The energy of compaction generates less modification at the microstructure level compared to the hydration. The rise in the water ratio from 0,5 to 0,6 generates an overall important modification:

The volume and intensity of the hysteresis are significantly reduced by hydration. For all configurations tested, this modification of the isotherm properties is accompanied by a generation of additional mesopore volume and a significant rise in SSA.

Considering non-activated dry mortars and w/b ratio, regardless of the compaction energy level, the pore size (mainly unimodal) distributions deviate towards larger pores when w/b increases. For activated dry mortars compacted at the optimal level of energy,

according to the activator used and its dosage, dry mortar microstructure varies differently at different level: specific surface change, hysteresis modification and the multimodal pore distribution.

The $Na_2CO_3$ activator with a dosage of 5% and a ratio w/b equals to 0.6 seems to be the optimal formulation. The $Na_2O_3Si$ with a dosage of 3% and a ratio w/b of 0.5 has given the best mechanical strength. Finally, the $CaCl_2$ activator shows a better microstructure with a dosage of 3% and a 0.5 w/b. The comparison between the UCS values obtained after the addition of the different activators results in the following ranking, from the best to the worst performance: $CaCl_2$ >$Na_2O_3Si$ > $Na_2CO_3$. Consideration of the elastic properties of the pores structure generated by each processed mixture could be an interesting issue to provide further information on the contrasting contribution of pore development on the mechanical strength of the material.

Further research on binding power and durability is recommended for this type of activated dry mortars including the grinding of WSA, i.e., the effect of particles size, the ratios of water to solids, of $SiO_2/Na_2O$ [43].

**Author Contributions:** Conceptualization, S.S., D.L. and A.R.; methodology, S.S., D.L. and A.R.; investigation, S.S.; writing—original draft preparation, S.S.; writing—review and editing, S.S., D.L. and A.R.; supervision, S.S., D.L. and A.R.; project administration, S.S., D.L. and N.S.; funding acquisition, N.S. All authors have read and agreed to the published version of the manuscript.

**Funding:** This research received no external funding.

**Institutional Review Board Statement:** Not applicable.

**Informed Consent Statement:** Informed consent was obtained from all subjects involved in the study.

**Data Availability Statement:** The data presented in this study are available on request from the corresponding author or the first co-author S.S.

**Acknowledgments:** The authors thank the Gustave Eiffel University for their support.

**Conflicts of Interest:** The authors declare no conflict of interest.

## References

1. Kumar, R.; Kumar, S.; Mehrotra, S.P. Towards sustainable solutions for fly ash through mechanical activation. *Resour. Conserv. Recycl.* **2007**, *52*, 157–179. [CrossRef]
2. Amit, S.K.S.; Islam, M.R. Application of paper sludge ash in construction industry: A review. In Proceedings of the 3rd International Conference on Civil Engineering for Sustainable Development (ICCESD2016), Khulna, Bangladesh, 12–14 February 2016; pp. 737–746, ISBN 978-984-34-0265-3.
3. Martínez-Lage, I.; Velay-Lizancos, M.; Vázquez-Burgo, P.; Rivas-Fernández, M.; Vázquez-Herrero, C.; Ramírez-Rodríguez, A.; Martín-Cano, M. Concretes and mortars with waste paper industry: Biomass ash and dregs. *J. Environ. Manag.* **2016**, *181*, 863–873. [CrossRef] [PubMed]
4. Cherian, C.; Siddiqua, S. Pulp and paper mill fly ash: A review. *Sustainability* **2019**, *11*, 4394. [CrossRef]
5. Logeswaran, V.; Ramakrishna, G. Waste paper sludge ash—State of art. *Int. J. Innov. Technol. Explor. Eng. (IJITEE)* **2019**, *8*, 2278–3075. [CrossRef]
6. Turner, T.; Wheeler, R.; Oliver, I.W. Evaluating land application of pulp and paper mill sludge: A review. *J. Environ. Manag.* **2022**, *317*, 115439. [CrossRef] [PubMed]
7. Vegas, I.; Gaitero, J.J.; Urreta, J.; García, R.; Frías, M. Aging and durability of ternary cements containing fly ash and activated paper sludge. *Constr. Build. Mater.* **2014**, *52*, 253–260. [CrossRef]
8. Agrawal, D.; Raut, S.P. Development of sustainable mortar from waste paper pulp ash. In *Proceedings of Sustainable Infrastructure Development & Management (SIDM)*; Elsevier: Amsterdam, The Netherlands, 2019. Available online: https://ssrn.com/abstract=3379024 (accessed on 25 April 2023). [CrossRef]
9. Al Zubaidi, A.B.; Ali, N.M.; Nasser, A.K. Study of the effect of recycled ash wastepaper on the mechanical properties of green concrete. In *IOP Conference Series: Materials Science and Engineering*; IOP Publishing: Bristol, UK, 2018; Volume 454. [CrossRef]
10. Kore, S.D.; Rajput, B.; Agarwal, A.; Pawar, A. Concrete made from waste paper sludge (WPS): A sustainable material. *Technol. Sustain.* **2023**, *2*, 188–205. [CrossRef]
11. Wong, L.S.; Chandran, S.N.; Rajasekar, R.R.; Kong, S.Y. Pozzolanic characterization of waste newspaper ash as a supplementary cementing material of concrete cylinders. *Case Stud. Constr. Mater.* **2022**, *17*, e01342. [CrossRef]

12. Zmamou, H.; Leblanc, N.; Levacher, D.; Kubiak, J. Recycling of high quantities of wastepaper sludge ash for production of blended cements and alternative materials. *Environ. Technol. Innov.* **2021**, *23*, 101524. [CrossRef]
13. Doudart de la Grée, G.C.H.; Yu, Q.L.; Brouwers, H.J.H. Upgrading and evaluation of waste paper sludge ash in eco-lightweight cement composites. *J. Mater. Civ. Eng.* **2018**, *30*, 04018021. [CrossRef]
14. Baloochi, H.; Aponte, D.; Barra, M. Soil stabilization using waste paper fly ash: Precautions for its correct use. *Appl. Sci.* **2020**, *10*, 8750. [CrossRef]
15. Bizjak, K.F.; Likar, B.; Mladenovič, A.; Serjun, V.Z. Valorized deinking paper residue as fill material for geotechnical structures. *Sci. Rep.* **2021**, *11*, 22363. [CrossRef]
16. Park, J.; Hong, G. Strength characteristics of controlled low-strength materials with waste paper sludge ash (WPSA) for prevention of sewage pipe damage. *Materials* **2020**, *13*, 4238. [CrossRef]
17. Xie, A. Optimization of wastepaper sludge ash (WSA) in robust cementitious systems. Ph.D. Thesis, University of Sherbrooke, Sherbrooke, QC, Canada, 2016; 331p. Available online: http://hdl.handle.net/11143/8859 (accessed on 25 April 2023).
18. Li, Z.; Ohnuki, T.; Ikeda, K. Development of paper sludge ash-based geopolymer and application to treatment of hazardous water contaminated with radioisotopes. *Materials* **2016**, *9*, 633. [CrossRef]
19. Pachamuthu, S.; Thangaraj, P. Effect of incinerated paper sludge ash on fly ash-based geopolymer concrete. *J. Građevinar* **2017**, *69*, 851–859. [CrossRef]
20. Owaid, H.M.; Al-Rubaye, M.M.; Al-Baghdadi, H.M. Use of waste paper ash or wood ash as substitution to fly ash in production of geopolymer concrete. *Sci. Rev. Eng. Environ. Sci.* **2021**, *30*, 464–476. [CrossRef]
21. Mavroulidou, M.; Shah, S. Alkali-activated slag concrete with paper industry waste. *Waste Manag. Res.* **2021**, *39*, 466–472. [CrossRef]
22. Mengasini, L.; Mavroulidou, M.; Gunn, M.J. Alkali-activated concrete mixes with ground granulated blast furnace slag and paper sludge ash in seawater environments. *Sustain. Chem. Pharm.* **2021**, *20*, 100380. [CrossRef]
23. Seifi, S.; Sebaibi, N.; Levacher, D.; Boutouil, M. Mechanical performance of a dry mortar without cement, based on paper fly ash and blast furnace slag. *J. Build. Eng.* **2018**, *22*, 113–121. [CrossRef]
24. Barrett, E.P.; Joyner, L.G.; Halenda, P.P. The determination of pore volume and area distributions in porous substances. *I. Computations from nitrogen isotherms. J. Am. Ceram. Soc.* **1951**, *73*, 373–380. [CrossRef]
25. Brunauer, S.; Emmett, P.H.; Teller, E. Adsorption of gases in multimolecular layers. *J. Am. Chem. Soc.* **1938**, *60*, 309–319. [CrossRef]
26. Das, G.; Razakamanantsoa, A.; Herrier, G.; Deneele, D. Influence of pore fluid-soil structure interactions on compacted lime-treated silty soil. *Eng. Geol.* **2021**, *296*, 106496. [CrossRef]
27. Das, G.; Razakamanantsoa, A.; Herrier, G.; Deneele, D. Physicochemical and microstructural evaluation in lime-treated silty soil exposed to successive wetting-drying cycles submitted to different testing conditions. *J. Mater. Civ. Eng.* **2023**, *35*, 04022458. [CrossRef]
28. Das, G.; Razakamanantsoa, A.; Herrier, G.; Deneele, D. Influence of wetting fluids on the compressive strength, physicochemical, and pore-structure evolution in lime-treated silty soil subjected to wetting and drying cycles. *Transp. Geotech.* **2022**, *35*, 100798. [CrossRef]
29. Das, G.; Razakamanantsoa, A.; Herrier, G.; Saussaye, L.; Lesueur, D.; Deneele, D. Evaluation of the long-term effect of lime treatment on a silty soil embankment after seven years of atmospheric exposure: Mechanical, physico-chemical, and microstructural studies. *Eng. Geol.* **2021**, *281*, 105986. [CrossRef]
30. Dailly, J. Valorisation de cendre volante papetière en techniques routières. In *Projet de Fin d'études en Génie Civil*; INSA: Strasbourg, France, 2017.
31. Fernandez-Jiménez, A.; Palomo, A. Composition and microstructure of alkali activated fly ash binder: Effect of the activator. *Cem. Concr. Res.* **2005**, *32*, 1984–1992. [CrossRef]
32. Hanjitsuwan, S.; Phoo-Ngernkham, T.; Li, L.; Damrongwiriyanupap, N.; Chindaprasirt, P. Strength development and durability of alkali-activated fly ash mortar with calcium carbide residue as additive. *Constr. Build. Mater.* **2018**, *162*, 714–723. [CrossRef]
33. Gailius, A.; Laurikietyte, Z. Waste paper sludge ash and ground granulated blast furnace slag a binder in concrete. *J. Civ. Eng. Manag.* **2003**, *9*, 198–202. [CrossRef]
34. Levacher, D.; Jain, S.; Pontus, P.; Seifi, S.; Haquin, S.; Bukasa Tshinkunku, E. A method to compact dry mortars made with by products. In Proceedings of the Geo-Environmental Engineering 2017, 16th Global Joint Seminar on Geo-Environmental Engineering, Seoul National University, Seoul, Republic of Korea, 18–20 May 2017; pp. 331–336.
35. Donohue, M.D.; Aranovich, G.L. Adsorption hysteresis in porous solids. *J. Colloid Interface Sci.* **1998**, *205*, 121–130. [CrossRef]
36. Radjy, F.; Sellevold, E.J.; Hansen, K.K. *Isosteric Vapor Pressure-Temperature Data for Water Sorption in Hardened Cement Paste: Enthalpy, Entropy and Sorption Isotherms at Different Temperatures*; Report Technical University of Denmark, BYG.DTU R-057; Technical University of Denmark: Lyngby, Denmark, 2003.
37. Thommes, M.; Katsumi, K.; Neimark, A.V.; Olivier, J.P.; Rodriguez-Reinoso, F.; Rouqueol, J.; Sing, S.W. Physisorption of gases, with special reference to the evaluation of surface area and pore size distribution (IUPAC Technical Report). *Pure Appl. Chem.* **2015**, *87*, 1051–1069. [CrossRef]
38. Sing, K.S.W. Reporting physisorption data for gas/solid systems. *Pure Appl. Chem.* **1982**, *54*, 2201–2218. [CrossRef]
39. Boher, C. Etude Expérimentale et Modélisation de la Diffusion Gazeuse à Travers des Milieux Poreux Partiellement Saturés en eau. Application aux Verres Vycor, Géopolymères et Pâte de Ciment CEM V. Ph.D. Thesis, INSA, Toulouse, France, 2012.

40. Baroghel-Bouny, V. Caractérisation Microstructurale et Hydrique des Pâtes de Ciment et des Bétons Ordinaires et à très Hautes Performances. Ph.D. Thesis, Ecole Nationale des Ponts et Chaussées, Paris, France, 1994. Available online: https://pastel.archives-ouvertes.fr/tel-00523299 (accessed on 25 April 2023).
41. Feldman, R. Influence of condensed silica fume and sand/cement ratio on pore structure and frost resistance of Portland cement mortars. *Spec. Publ.* **1986**, *91*, 973–990.
42. Musy, A.; Soutter, M. *Physique du Sol*; PPUR Presses Polytechniques: Lausanne, Switzerland, 1991; Volume 6, 348p.
43. Newman, A.; Halim, N.I.; Sidek, M.N.M.; Saman, H.M.; Alisibramulisi, A. Enhancement of high strength concrete performance by utilising nano waste paper sludge ash. *Sci. Res. J.* **2021**, *18*, 89–101. [CrossRef]

**Disclaimer/Publisher's Note:** The statements, opinions and data contained in all publications are solely those of the individual author(s) and contributor(s) and not of MDPI and/or the editor(s). MDPI and/or the editor(s) disclaim responsibility for any injury to people or property resulting from any ideas, methods, instructions or products referred to in the content.